WILEY

ORIGINAL RESEARCH

Hyperspectral anomaly detection via memory-augmented autoencoders

Zhe Zhao[1] | Bangyong sun[1,2]

[1]Faculty of Printing, Packaging Engineering and Digital Media Technology, Xi'an University of Technology, Xi'an, China

[2]Norwegian Colour and Visual Computing Laboratory, Norwegian University of Science and Technology, Gjovik, Norway

Correspondence

Bangyong sun, Faculty of Printing, Packaging Engineering and Digital Media Technology, Xi'an University of Technology, Xi'an, China.
Email: sunbangyong@xaut.edu.cn

Abstract

Recently, the autoencoder (AE) based method plays a critical role in the hyperspectral anomaly detection domain. However, due to the strong generalised capacity of AE, the abnormal samples are usually reconstructed well along with the normal background samples. Thus, in order to separate anomalies from the background by calculating reconstruction errors, it can be greatly beneficial to reduce the AE capability for abnormal sample reconstruction while maintaining the background reconstruction performance. A memory-augmented autoencoder for hyperspectral anomaly detection (MAENet) is proposed to address this challenging problem. Specifically, the proposed MAENet mainly consists of an encoder, a memory module, and a decoder. First, the encoder transforms the original hyperspectral data into the low-dimensional latent representation. Then, the latent representation is utilised to retrieve the most relevant matrix items in the memory matrix, and the retrieved matrix items will be used to replace the latent representation from the encoder. Finally, the decoder is used to reconstruct the input hyperspectral data using the retrieved memory items. With this strategy, the background can still be reconstructed well while the abnormal samples cannot. Experiments conducted on five real hyperspectral anomaly data sets demonstrate the superiority of the proposed method.

1 | INTRODUCTION

Hyperspectral image (HSI) is a 3-D cube data [1], where the two dimensions reflect the spatial structure of the land cover and another dimension provides hundreds of spectral bands. Benefitted from the rich spectral–spatial information [2], HSI has been widely used for change detection [3, 4], classification [5–10], unmixing [11, 12], and anomaly detection [13–15]. Anomaly detection in HSI (HAD) has drawn much attention due to its significance in military surveillance and mineral exploration [16]. Normally, anomalies are significantly different from their surrounding pixels in the spectral or spatial domain. Thus, hyperspectral anomaly detection often refers to finding anomalies within the HSI by comparing the anomaly-restrain reconstructed background and the original image.

To detect anomalies effectively, the researchers designed various detectors from different perspectives. The statistical modelling-based methods assume the HSI obeys a certain statistical distribution, for example, Gaussian normal distribution, and the background can be estimated using the statistical variables [17]. The Reed-Xiaoli detector (RX) [18] detected anomalies by calculating the Mahalanobis distance between the target pixel and background pixels. Afterwards, numerous variants of RX based methods are proposed, such as the local RX detector (LRX) [19], kernel RX detector (KRX) [20], and weighted RX detector [21]. Recently, a higher-order statistics-based method was proposed for HAD in Ref. [22]. Specifically, the distribution of the target and background is modelled by Adaptive Cosine Estimation based statistical hypothesis, and the higher-order statistics are used to replace the mean and covariance matrix in the original RX detector. To improve the accuracy of the KRX detector, the Fourier features and the Nystrom approach were used in Ref. [23]. However, the multivariate Gaussian distribution of the background may not be reasonable due to the complex scenes in

the real world [24] and usually results in lower detection accuracy in a certain background.

To avoid distribution errors, the representation modelling-based methods use spatial neighbourhoods to represent the background pixel [17, 25–27]. The background joint sparse representation [25] method is a typical sparse representation-based method, which represents background samples by using an overcomplete dictionary. Li and Du first introduce the collaborative representation theory (CRD) into the HAD domain [26], and the authors use neighbourhood pixels to represent the centre pixel, then reconstruction errors are employed to detect anomalies. To reduce computing time, Ma et al. [27] designed a fast CRD method. The original CRD detector assumes that each band has an equal contribution during the collaborative representation, but the case is not reasonable in practical applications. To alleviate this issue, Wang et al. [17] designed a new objective function by combining weight learning and collaborative representation. Due to the superiority of the deep network, a novel hyperspectral anomaly detection method that combines stacked autoencoder (AE) and CRD is proposed in Ref [28]. The encoder is constrained by a collaborative representation during feature extraction, and then the preliminary detection result is obtained by using CRD on the acquired features. Finally, a carefully designed anomaly detection procedure is used to improve the detection accuracy. For most CRD based methods, the appropriate window size is difficult to choose [29].

The matrix decomposition modelling-based methods assume that background pixels have low-rank property, and anomalies are sparsely distributed in the HSI scenes. Zhang et al. [30] decomposed HSI into a low-rank part and sparse part, then the anomalies are detected by using Mahalanobis distance on the sparse part. Xu et al. [31] estimated the background by adopting a background dictionary, and the anomalies appear as the response of the residual matrix. Qu et al. [32] proposed a spectral unmixing-based anomaly detector, which combined the unmixing method and dictionary learning for HAD. Considering the correlation of adjacent bands in HSI, a spectral difference low-rank representation learning framework for HAD was proposed in Ref. [33]. Specifically, the difference of the dictionary is obtained by the residual of adjacent bands, in which the redundancy of adjacent bands and low rankness of the background are considered. Different from previous low-rank and sparse decomposition-based models, Feng et al. [34] detect anomalies utilising both the sparse part and the low-rank part. For most matrix decomposition-based methods, the parameters are difficult to determine due to the lack of prior knowledge about anomalies or background [17, 35].

Recently, deep learning has achieved good results on a variety of visual tasks [36–38], and it has also shown superiority in HSI processing [39, 40], especially for classification, denoising, unmixing [11], and anomaly detection [3, 41]. Based on the fact that anomalies usually occur with a lower probability compared with normal samples, the AE network is mainly trained by the normal samples, and the reconstruction errors with the AE network can be seen as the abnormal score

[42]. A stacked denoising autoencoder (SAE) for hyperspectral anomaly detection is proposed in Ref. [43], which uses SAE to estimate the background. Zhao and Zhang [44] proposed a method named LRaSMD-SSSAE for HAD in which the matrix decomposition and AE are combined into a joint framework. Chang et al. [45] applied sparse AE for HAD through a dual concentric window. To further use spectral–spatial information, Lei et al. [46] utilised a deep brief network and attribute filter for HAD. Wang et al. [17] utilised the skip connections for the encoder and decoder, and an adaptive weighted loss is designed to punish the anomaly reconstruction. Sun et al. [47] used 3D convolutional AE for feature extraction, and anomalies are separated from the feature image. Zhang et al. [48] designed a 3D variational AE for HAD. Lu et al. [13] used the manifold learning skill to constrain the processing of the encoder for HAD, which achieves promising results by combining the local and global reconstruction errors. Jiang et al. [1] proposed an algorithm based on generative adversarial network. For better learning the distribution of background, the multivariate Gaussian distribution was applied to the encodings of the encoder through a discriminator. Concurrent to this method, a semi-supervised AE-based adversarial learning was proposed in Ref. [49]. The distribution of background is estimated by the generative adversarial network, and the anomalies are detected via Mahalanobis distance in the reconstructed data. Adversarial autoencoders for HAD were proposed in Ref. [50], and the preliminary result is obtained by removing the background of the latent representation. Then the Mahalanobis distance is used for anomaly detection on the rectified data. From these literature, it can be seen that the major challenge for HAD is how to accurately represent the background without the anomalies. However, due to the high dimensionality and redundant information of the complex image scenes, it's always hard to represent the background well.

Although the previous AE-based methods have achieved promising results, a common issue has been ignored. As shown in Figure 1, when the AE generalises very well or the decoder is too strong, the abnormal samples may also be well reconstructed [51]. In this case, abnormal samples have lower reconstruction errors and often results in the failure of detecting anomalies. To further improve the detection accuracy, it is beneficial to guide the AE to generate large reconstruction errors for anomalies. In this paper, a memory module is introduced into the AE architecture for hyperspectral anomaly detection [51], where the memory items are used to record the prototypical patterns of background spectral samples. In this way, the augmented AE can still reconstruct the background well but not for the anomalies, thus the anomalies can be detected by checking the reconstruction errors. The whole scheme of the memory-augmented autoencoder for hyperspectral anomaly detection (MAENet) consists of three steps: First, the encoder extracts features from the hyperspectral images, and then the encodings as query features are applied to retrieve the most similar items in the memory module. Finally, the selected items are used as the input for the decoder to reconstruct the hyperspectral data.
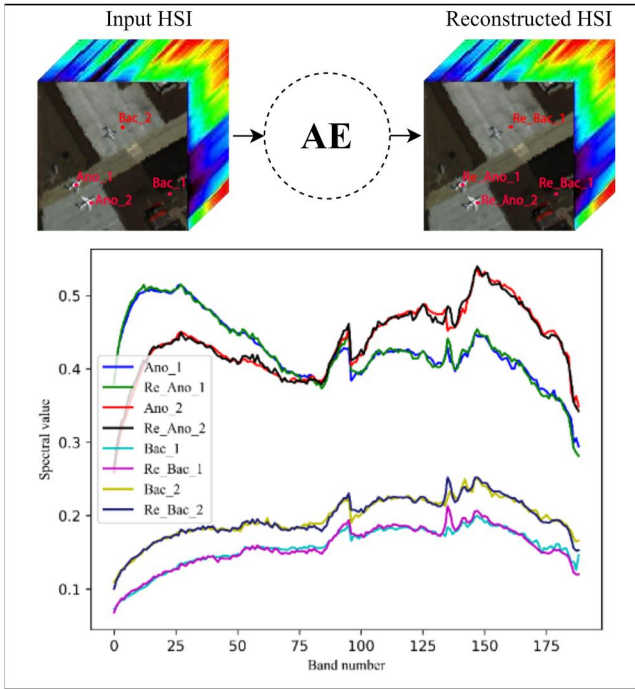
FIGURE 1 The abnormal samples can be reconstructed well using the traditional autoencoder (AE) based method. In this case, the detection accuracy is limited by using reconstruction errors. The Ano_i denotes ith abnormal pixel, and Bac_i is ith background pixel. The Re_Ano_i and Re_Bac_i represent the reconstructed spectral pixel

The major contributions of MAENet are threefold:

1. A new hyperspectral anomaly detector is proposed based on memory-augmented autoencoders. Specifically, a memory module is used to record the prototypical patterns of background spectral samples, and the background can be reconstructed well but not for anomalies.
2. To further highlight the reconstruction errors of anomalies, the L2 distance between latent representation and retrieved items is added into the traditional mean square error (MSE) loss. Thus, the consistency of background samples can be preserved, which is beneficial for anomaly detection.
3. To demonstrate the superiority of the MAENet, the comparison experiment with an ablation study was conducted on five real hyperspectral data sets with seven methods, and the MAENet obtained promising AUC values.

The rest of this paper is organised as follows: The proposed MAENet is introduced in Section 2. The parameter analysis and detection results are show in Section 3. Section 4 gives the conclusions.

2 | PROPOSED METHOD

In this paper, a memory-augmented AE network is proposed for hyperspectral anomaly detection (MAENet). The background of the HSI is reconstructed by the AE augmented with a memory module [51], and the anomalies are then represented as reconstruction errors. The overall architecture of the MAENet is shown in Figure 2. Given an input spectral sample, the encoder first transforms it into a latent representation also named query feature. Then, the query feature is used to retrieve fewer but the most relevant items in the memory module by using an attention-based sparse addressing operator. Theoretically, the anomalies have low probabilities of being reconstructed by those selected background-relevant samples. Finally, the retrieved items are used as the input for decoder to reconstruct the input HSI, and the anomalies can be detected by comparing the input and reconstructed HSI. To better represent the encodings of background spectral samples and suppress the abnormal encodings, a self-perception loss consisting of one original pixel-level spectral reconstruction term and one high-level latent reconstruction term is designed. Accordingly, the consistency of background samples between latent representation and retrieved feature is preserved, while the anomalies are not.

Table 1 listed the architecture of the AE in the proposed method. The architecture of the decoder is symmetric with the encoder, except for removing the LReLu activation function in the last layer. Each part has three layers, and every layer contains a fully connected component, a batch normalisation component and LReLu activation function. The encoder aims to convert the complex high-dimensional hyperspectral data into low-dimensional informative latent representation, which is also named query feature. Then, the query feature is used to search for the most similar items in the memory module, and those selected items are used by the decoder to reconstruct the input HSI. In Table 1, d denotes the hidden nodes of the last layer in the encoder, which is important for the network. Session 3.4 will show the effect of final detection accuracy in detail.

2.1 | Encoder-decoder architecture

Let $\mathbf{X} \in \mathbb{R}^{D \times M}$, $\widehat{\mathbf{X}} \in \mathbb{R}^{D \times M}$, and $\mathbf{Z} \in \mathbb{R}^{d \times M}$ represent the input hyperspectral data, reconstructed data, reconstructed data, and the latent representation, respectively. D and d stand for the channel of input data and latent data, and M represents the total number of pixels in the HSI. The workflow of MAENet to reconstruct the HSI data can be expressed as follows:

$$\mathbf{Z} = f_e(\mathbf{X};\ \theta_e, b_e) \tag{1}$$

$$\widehat{\mathbf{X}} = f_d\left(\widehat{\mathbf{Z}};\ \theta_d, b_d\right) \tag{2}$$

where θ_e and θ_d denote the weight matrixes, b_e and b_d are the bias terms, $f_e\ (\cdot)$ and $f_d\ (\cdot)$ represent the encoder and decoder, respectively. Normally, when the latent representation $\mathbf{Z}$ is directly used as the input for decoder to reconstruct the HSI, the anomalies may also be reconstructed well due to the good generalisation performance of AE. In this paper, a memory module is built to record various prototypical patterns of
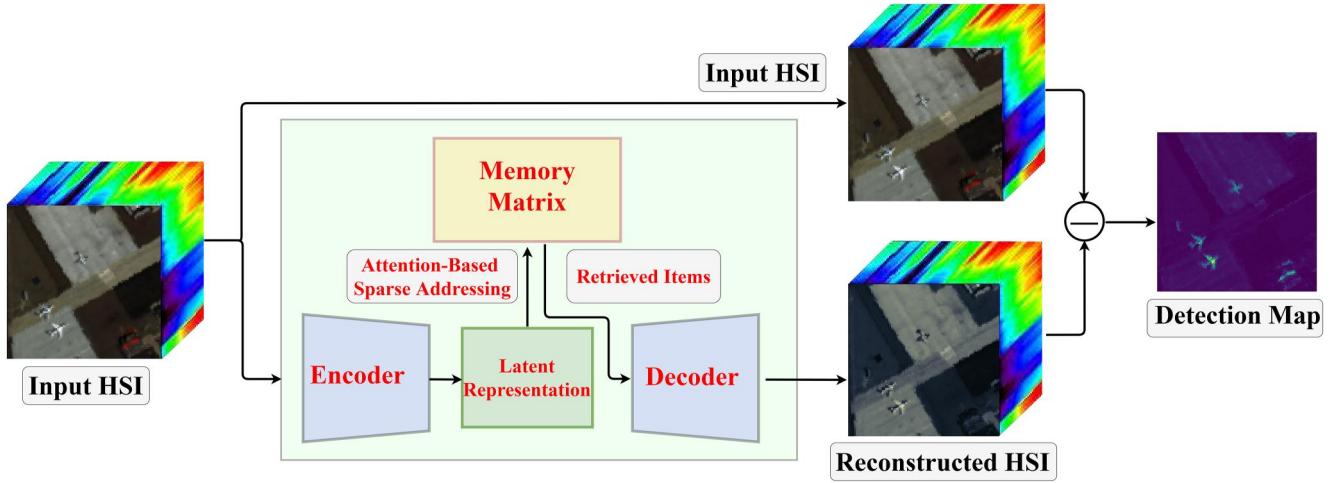
FIGURE 2 Flowchart of the proposed MAENet

background encodings during the training phase, and the encodings act as the query features to search for the most relevant items $\widehat{\mathbf{Z}}$ in the memory module. Finally, $\widehat{\mathbf{Z}}$ as the input for decoder is used to reconstruct the input hyperspectral data.

There are two cases for the representations (encodings): abnormal or normal. Since the memory matrix is initialised with a Gaussian distribution and forced by self-perception loss, it can record the prototypical patterns of the background. If the encodings are normal, it will have strong correlations with memory items. Then, the retrieved items tend to be background samples. Otherwise, the input samples are anomalies, just a few but the most relevant samples because the memory items are similar to normal samples. Therefore, anomalies have high reconstruction errors compared with normal samples, and the reconstruction errors are then used for anomaly detection.

2.2 | Memory module

The memory module in the proposed method is built to search for the prototypical patterns of the background encodings, and the latent representations generated from the encoder are used as query features to retrieve fewer but the most relevant items in the memory module by using an attention-based sparse addressing operator. Then, those items are put into the decoder to reconstruct the original HSI. Figure 3 shows the process of the attention-based sparse addressing operator.

As shown in Figure 3, the memory module is a matrix $\mathbf{M} \in \mathbb{R}^{N \times d}$, which contains N vectors with the same dimension d as latent representation. N defines the capacity of the memory matrix to describe the background, which should well represent all the background categories. Similar to the dictionary-learning approach, the memory matrix is essentially a dictionary, but it is updated in an end-to-end fashion by using back-propagation. In Ref. [52], the author shows that the closer the background resembles a Gaussian distribution, the better

TABLE 1 Detailed features for experimental data sets

Layer	Configuration
Encoder1	Hidden nodes: 128
	BN + ReLu
Encoder2	Hidden nodes: 64
	BN + ReLu
Encoder3	Hidden nodes: d
	BN + ReLu
Decoder1	Hidden nodes: 64
	BN + ReLu
Decoder2	Hidden nodes: 128
	BN + ReLu
Decoder3	Hidden nodes: *input channel*
	BN + ReLu

the performance of hyperspectral anomaly detection. Inspired by this, the memory matrix is initialised by Gaussian normal distribution, and it upgrades with the parameters of the AE network during the training phase. The parameter of N will be discussed in Section 3.4.

Let $\{z_i\}_{i=1}^{M} \in \mathbb{R}^{d \times 1}$ denote the $i-th$ query feature of $\mathbf{Z}$, and the row vector $\{m_j\}_{j=1}^{N} \in \mathbb{R}^{1 \times d}$ denote the $j-th$ row of $\mathbf{M}$. Based on the inherent spectral characteristics of hyperspectral vectors, the cosine similarity between the memory items and the query features is used to construct the initial addressing matrix. The cosine similarity is defined as:

$$d(z_i, m_j) = \frac{z_i m_j^T}{\|z_i\| \|m_j\|} \tag{3}$$

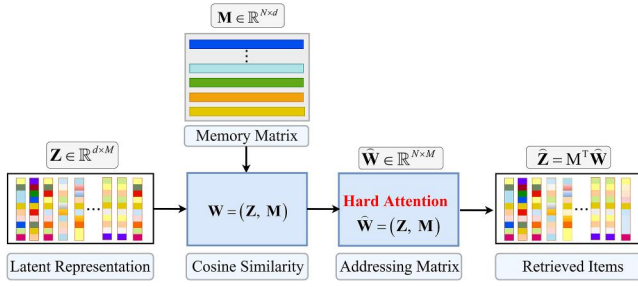In order to keep the addressing weight having physical meaning, the softmax operator is applied to w_j:

FIGURE 3 Procedure of attention-based sparse addressing operator

$$w_j = \frac{\exp\big(d(z_i, \, m_j)\big)}{\sum_{j=1}^{N} \exp\big(d(z_i, \, m_j)\big)} \qquad (4)$$

Equation 4 shows that the more similar the query features with memory items, the bigger the value of w_j. Thus, the retrieved memory items $\widehat{\mathbf{Z}}_i$ with w_j can be obtained as follows:

$$\widehat{\mathbf{Z}}_i = \mathbf{WM} = \sum_{j=1}^{N} w_j m_j \qquad (5)$$

From Equations 3, 4 and 5, the query features (i.e. encoding features) can be represented by memory items. The aim of the memory module is to record various prototypical patterns of the background encodings, and the normal query features can be well represented by memory items, while the abnormal query features cannot. However, because of the powerful generalisation of AE and the mixed pixels existing in HSI (the abnormal pixels have some common characteristics with normal pixels), the anomalies may still have possibilities to be represented with a complex combination of memory items. In this case, the anomalies will correspond to small reconstruction errors and make it difficult to distinguish from background samples. In order to alleviate this issue, a hard attention mechanism is introduced for addressing vector w_j [51]:

$$\widehat{w}_j = \frac{\max\big(w_j - \delta, \, 0\big) \cdot w_j}{|w_j - \delta| + \varepsilon} \qquad (6)$$

where δ denotes the threshold, and the items with similarity bigger than δ are used to construct the addressing matrix. In this way, there is no need to use dense combinations of memory items to represent the query feature. The effect of δ for the final detection result is discussed in Section 3.4. The ε is a smaller positive scalar, which keeps the denominator from being zero. Finally, the modified addressing vector $\widehat{w}_j$ is used to retrieve memory items:

$$\widehat{\mathbf{Z}}_i = \widehat{w}\mathrm{M} = \sum_{j=1}^{N} \widehat{w}_j m_j \qquad (7)$$

$\widehat{\mathbf{Z}}_i$ denotes the final retrieved memory items of the $i-th$ query feature, which is used to reconstruct the input HSI by the decoder.

2.3 | Training loss and abnormal detection

To better highlight the anomalies and suppress the background, a self-perception loss comprising two items is designed for training the network. As shown in Equation 8, the first term is the original pixel level reconstruction loss, and another one is the high-level latent reconstruction loss. For the hyperspectral dataset $\{x_i\}_{i=1}^{M}$ with M samples, let $\{\widehat{x}_i\}_{i=1}^{M}$, $\{z_i\}_{i=1}^{M}$ and $\{\widehat{z}_i\}_{i=1}^{M}$ denote the reconstructed samples, latent representation, and retrieved memory items, respectively. The loss functions can be formulated as:

$$L(\theta_e, \theta_d, \mathrm{M}) = \frac{1}{M} \sum_{i=1}^{M} \bigg(\big\|x_i - \widehat{x}_i\big\|_2^2 + \lambda \big\|z_i - \widehat{z}_i\big\|_2^2 \bigg) \qquad (8)$$

where λ is a weight parameter, which is used to balance two items during the training procedure. The effect of λ will be further discussed in Section 3.4.

When the network converges, the MSE is applied as s, the criterion for anomaly detection:

$$e(i) = \frac{1}{D} \sum_{d}^{D} \big\|x_i^d - \widehat{x}_i^d\big\|_2^2 \qquad (9)$$

where $e(i)$ denotes the abnormality score of the $i-th$ pixel, and D represents the dimension of input HSI. Compared with the abnormal samples, the normal samples are more similar to the retrieved features, which correspond to small reconstruction errors. Thus, the reconstruction errors can be used to detect the anomalies.

3 | EXPERIMENTS

3.1 | Data sets

Five real-world HSIs are used in our experiments, the details are listed in Table 2.

1. **AVIRIS-I Data Set**: This HSI is commonly used by many previous works, and it was collected by the Airborne Visible/Infrared Imaging Spectrometer (AVIRIS) sensor. The original image is 400×400 pixels, including 224 spectral channels in the range 366–2496nm. In our experiments, a sub-image with the size of 100×100 pixels are applied for the test and denoted as AVIRIS-I [30], Consistent with previous literature, the bad bands are removed. The details of AVIRIS-I are listed in the first row of Table 2, and the image scene and ground truth (GT) are shown in Figure 4a and 4f.

T A B L E 2 Detailed features for experimental datasets

HSIs	Captured place	Sensor	Resolution	Spatial size	Experimental bands	Target size	Type
AVIRIS-I	San Diego	AVIRIS	3.5 m	100×100	189	57 pixels	aeroplanes
AVIRIS-II	San Diego	AVIRIS	3.5 m	100×100	189	134 pixels	aeroplanes
EI Segundo	Segundo	AVIRIS	7.1 m	250×300	224	2048 pixels	tanks
Texas Coast	Texas Coast	AVIRIS	17.2 m	100×100	207	155 pixels	buildings
Los Angeles-3	Los Angeles	AVIRIS	7.1 m	100×100	205	170 pixels	aeroplanes

2. **AVIRIS-II Data Set:** The size of the AVIRIS-II data set is 100×100 pixels, and three aeroplanes with 134 pixels are regarded as anomalies. The pseudo colour image and GT are shown in Figure 4b and 4g, respectively.

3. **EI Segundo Data Set:** The channel of this HSI is 224, and the spatial size of it is 250×300. The storage tanks and the towers occupying 2048 pixels in the oil refinery are regarded as anomalies. The pseudo colour image and GT are shown in Figure 4c and 4h.

4. **Texas Coast Data Set:** The Texas coast data set has 207 spectral bands, and the wavelengths range from 0.45 to 1.35 μm. The spatial size is 100×100 pixels, and the spatial resolution is 17.2 m/pix. The total of 155 pixels are regarded as anomalies, and the pseudo colour image and GT are shown in Figure 4d and 4i.

5. **Los Angeles-3 Data sets:** The last data set comes from Ref. [53], which is captured by the AVIRIS sensor. In the image, the airports are regarded as anomalies. The size of this data set is 100×100, and band number is 205. The pseudo colour image and GT are shown in Figure 4e and 4j.

3.2 | Comparison detectors and evaluation criterion

In our experiments, the receiver operating characteristic (ROC) curve and the area under the curve (AUC) are shown as two evaluation indicators [54]. Seven typical HAD methods are employed to compare with our proposed MAENet. The RX and LRX detectors are statistical-based methods, and the CRD detector is a representation-based method. The low-rank and sparse representation detector (LRASR) belongs to one of the decomposition-based methods, and the deep autoencoder anomaly detector (DAEAD) detects anomalies in the AE framework. The kernel isolation forest detector (KIFD) is a recently proposed detection method, and the attribute filter based detector (AED) is an efficient detector. Specifically, the DAEAD method and the proposed method are implemented based on the TensorFlow framework, and the other five methods are implemented by MATLAB 2018b. For the MAENet, the number of epochs is 50, and the learning rate is 0.0001. The BatchSize for AVIRIS-I and AVIRIS-II is 64, and the other data sets equal their pixel number. Furthermore, the optimiser is Adam [55].

The compared detectors are introduced as follows:

1. The GRX (it is also named RX) detector is commonly used for comparison, which detects anomalies by estimating the global background statistics [18].

2. The LRX detector is the local version of the RX method [19]. The performance of LRX is sensitive to the sliding double window sizes (w_{in} and w_{out}). In the experiment, the w_{in} is ranging from 3 to 39 and w_{out} is ranging from 5 to 55. The optimal window size is set as (13, 25), (37, 55), (9, 31), (17, 19), and (15, 9) for the AVIRIS-I, AVIRIS-II, EI Segundo, Texas Coast and Los Angeles-3 data sets, respectively.

3. The CRD detector assumes that the background samples can be represented by their local neighbourhood, while anomalies cannot [26]. Following the LRX method, the optimal window sizes of the CRD method are set as (19, 23), (39, 51), (13, 31), (23, 35), and (9, 7) for the AVIRIS-I, AVIRIS-II, EI Segundo, Texas Coast and Los Angeles-3 data sets, respectively, and the regularisation parameter λ is set as original paper.

4. The LRASR detector decomposes HSI into a low-rank part and a sparse part through dictionary learning, and anomalies are determined by L1 norm in the sparse part [31].

5. The DAEAD detector is an AE-based method and the abnormal score is calculated from the reconstruction errors [56].

6. The KIFD detector assumes that anomalies rather than the background can be easily separated in the kernel space, and the anomalies are detected by a recursive framework [57].

7. The AED detector uses the attribute filter and edge-preserve filter for anomaly detection, and their detection results were convincing [53].

3.3 | Parameters analysis

The main parameters in MAENet include the number of items N in the memory matrix, the shrinkage threshold δ, the weight parameter λ in the loss function, and the hidden nodes d of the AE network.

(1) *The parameters of d and λ.* The effect of d and λ for final detection accuracy is shown in Figure 5, in which the y-axis is the AUC scores that used to reflect the effect of different parameter settings. The number of hidden nodes d is an essential parameter for the AE network, and d is changing from 6 to 36. As shown in Figure 5a, with the
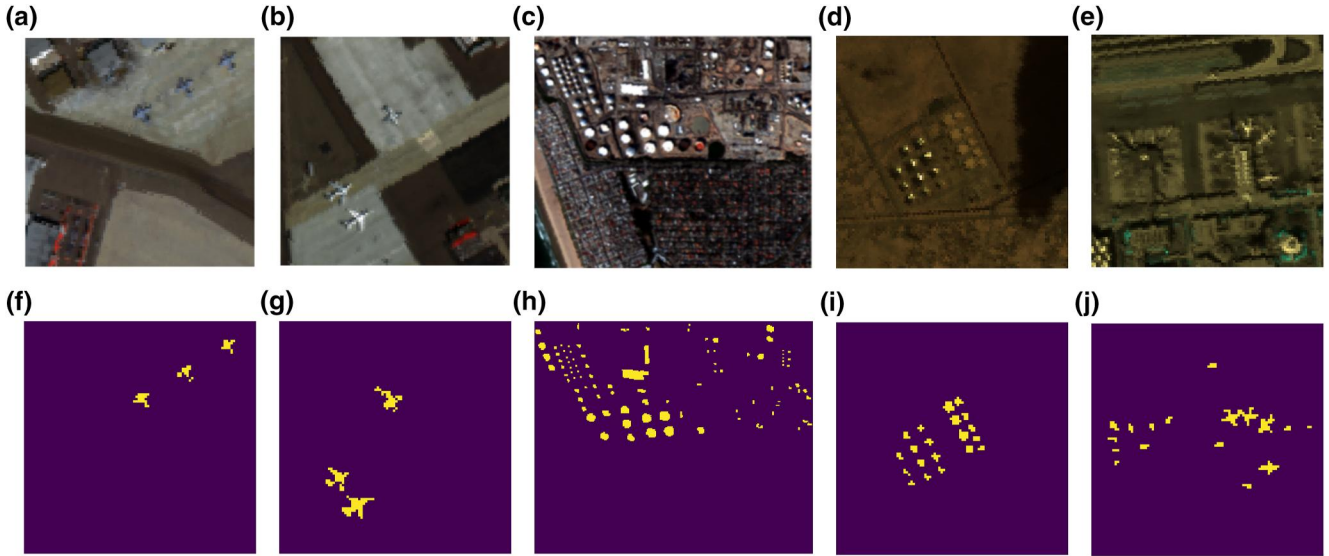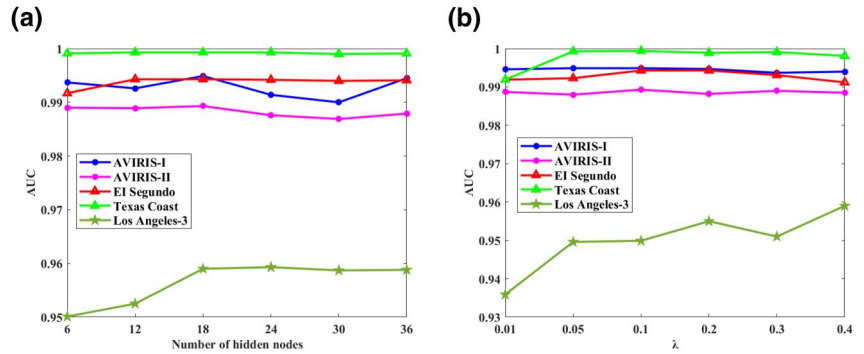
FIGURE 4 Data sets and ground truth (GT). (a)–(e) are the Pseudo-colour images of the AVIRIS-I, AVIRIS-II, EI Segundo, Texas Coast and Los Angeles-3 data sets, respectively. (f)–(j) are the corresponding GT of those data sets

FIGURE 5 The effect of the parameters for final detection accuracy. (a) Number of hidden nodes. (b) Weight parameter λ

increase of the number of hidden nodes, the AUC tends to rise, and it begins to decrease when d is greater than 18. In addition, the weighted parameter λ balances the effect of the high-level latent reconstruction term in the loss function during the training phase. As shown in Figure 5b, when λ is bigger than 0.1, the AUC values of the AVIRIS-II and Texas Coast data sets become stable, but the detection accuracy is decreasing for the EI Segundo and AVIRIS-II data set. For the Los Angeles-3 data set, a larger λ can obtain a better result. Thus, the optimal d is chosen as 18, and $\lambda = 0.4$ for the Los Angeles-3 data set, the other data sets are set as 0.1.

(2) *The parameter of N and δ.* The number of items N in the memory matrix determines how many items should represent the latent features, and the shrinkage threshold δ prevents dissimilar items from representing encoding features. Let N be set from [160, 240, 320, 400, 480], and δ be chosen from [1/N, 1.5/N, 2/N, 2.5/N, 3/N]. Figure 6a-e show the effect of different combinations of N and δ for the AVIRIS-I, AVIRIS-II, EI Segundo, Texas Coast and Los Angeles-3 data sets, respectively. The AVIRIS-I, AVIRIS-II, EI Segundo and Angeles-3 data sets

are stable under different parameter settings, and the Texas Coast data set achieves the promised result in suitable (N, δ). The MAENet obtained a considerable performance for all data sets when N and δ are set 320, 2/N, respectively.

3.4 | 3.4 detection performance

The detection maps, ROC curves, and AUC scores for the eight detectors are shown in Figures 7–12 and Table 3, respectively. The MAENet shows satisfactory performances compared with other methods, and the AUC scores are highest for three data sets.

(1) *Detection Results on AVIRIS-I Data Set.* Figure 7 shows the abnormal maps for the AVIRIS-I data set. GRX and LRX methods suppress the background well, but they almost cannot detect the anomalies. Compared with the RX detector, the CRD and DAEAD detect more abnormal targets, but many background pixels are detected as anomalies. The LRASR, KIFD, AED and MAENet can recognise almost all anomalies, with the shapes and
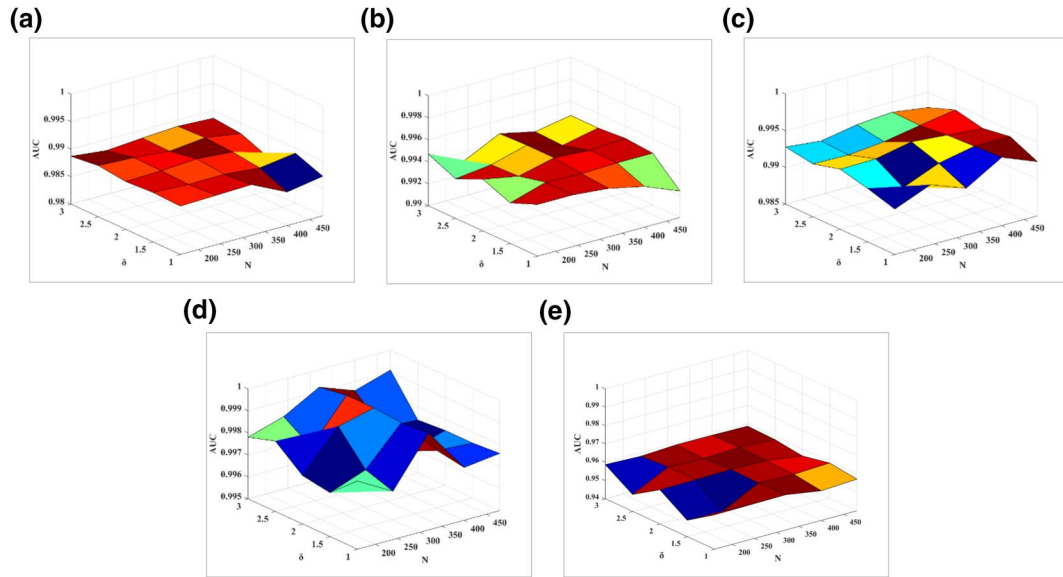
FIGURE 6 The effect of the number of items N in the memory matrix and the shrinkage threshold δ. (a) AVIRIS-I data set. (b) AVIRIS-II data set. (c) EI Segundo data set. (d) Texas Coast data set. (e) Los Angeles-3 data set
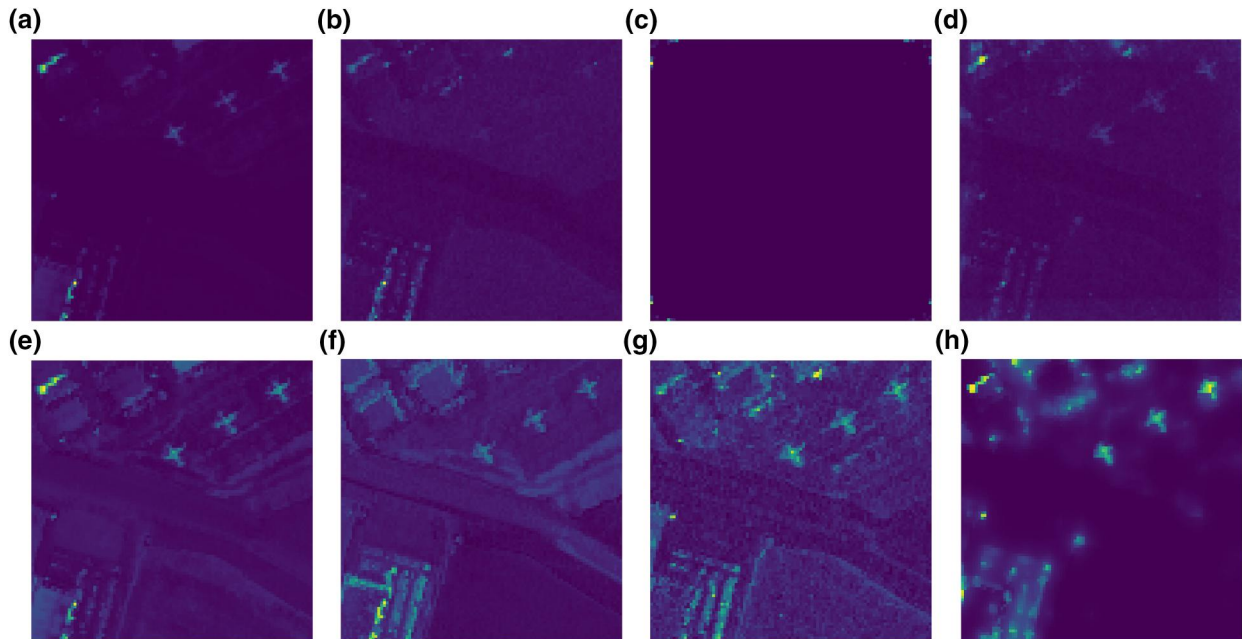

FIGURE 7 Detection maps on the AVIRIS-I data set. (a) memory-augmented autoencoder for hyperspectral anomaly detection (MAENet). (b) GRX. (c) local RX detector (LRX). (d) collaborative representation theory (CRD). (e) LRASR. (f) DAEAD. (g) KIFD. (h) AED

locations of anomalies clearly preserved. Compared with LRASR and KIFD, the MAENet and AED can better suppress the background. The abnormal-background separation map of the AED algorithm is more obvious, so the visual perception is better than the proposed algorithm.

To better illustrate the superiority of the proposed MAE-Net, the ROC curves of the eight methods are shown in Figure 12a. The curve of the MAENet and AED is higher than the curves of the GRX, LRX, CRD, and DAEAD methods.

But there are some crossovers among LRASR, KIFD, AED and the MAENet, thus, it cannot be used to judge which method performs better directly. Moreover, to judge the performance quantitatively, the AUC values are listed in Table 3. The table shows that LRASR, KIFD, AED and MAENet are larger than 0.98, and AED gets the highest AUC value, 0.9919, and our MAENet is 0.9894.

(2) *Detection Results on AVIRIS-II Data Set.* The detection results of the AVIRIS-II data set are shown in Figure 8. The LRX and CRD methods lost their capacity to detect
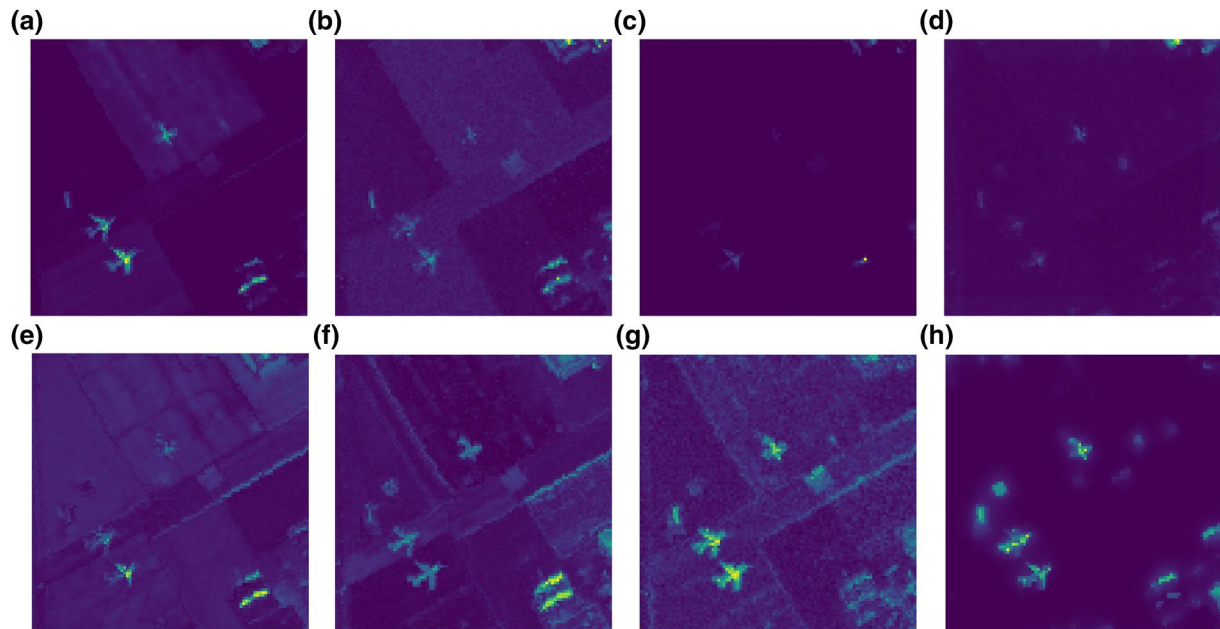
FIGURE 8 Detection maps on the AVIRIS-II data set. (a) memory-augmented autoencoder for hyperspectral anomaly detection (MAENet). (b) GRX. (c) local RX detector (LRX). (d) collaborative representation theory (CRD). (e) LRASR. (f) DAEAD. (g) KIFD. (h) AED

FIGURE 9 Detection maps on the EI Segundo data set. (a) memory-augmented autoencoder for hyperspectral anomaly detection (MAENet). (b) GRX. (c) local RX detector (LRX). (d) collaborative representation theory (CRD). (e) LRASR. (f) DAEAD. (g) KIFD. (h) AED
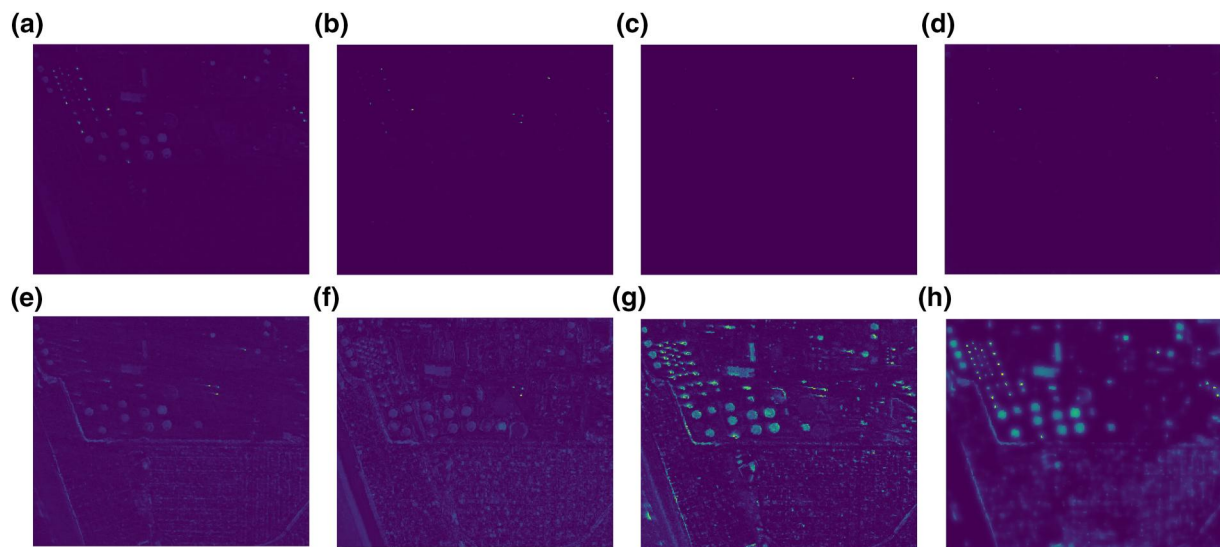
abnormal targets due to the complex image scenes. Meanwhile, some background pixels are mixed with anomalies. The LRASR and GRX methods can accurately detect the positions of the anomalies, but the shapes of the abnormal objects are blurred. The DAEAD method can detect most anomalies but cannot suppress the background in the bottom right corner of the image. The contrast between aeroplanes and the background of the KIFD, AED and MAENet is high, but the anomaly targets detected by MAENet are relatively clearer than KIFD and AED, which indicates the superiority of the proposed

method. As shown in Figure 12b, the ROC curves of KIFD and MAENet are higher than the curves of the other compared methods, which validates the effectiveness and advantage of MAENet again. There is a crossover between KIFD and MAENet. To further judge the performance between KIFD and MAENet, the AUC values are listed in Table 3. From the third Column of Table 3, it can be seen that memory-augmented autoencoder for hyperspectral anomaly detection (MAENet) gets the highest AUC value, 0.9949, while the KIFD obtains the second-highest AUC value, 0.9912.
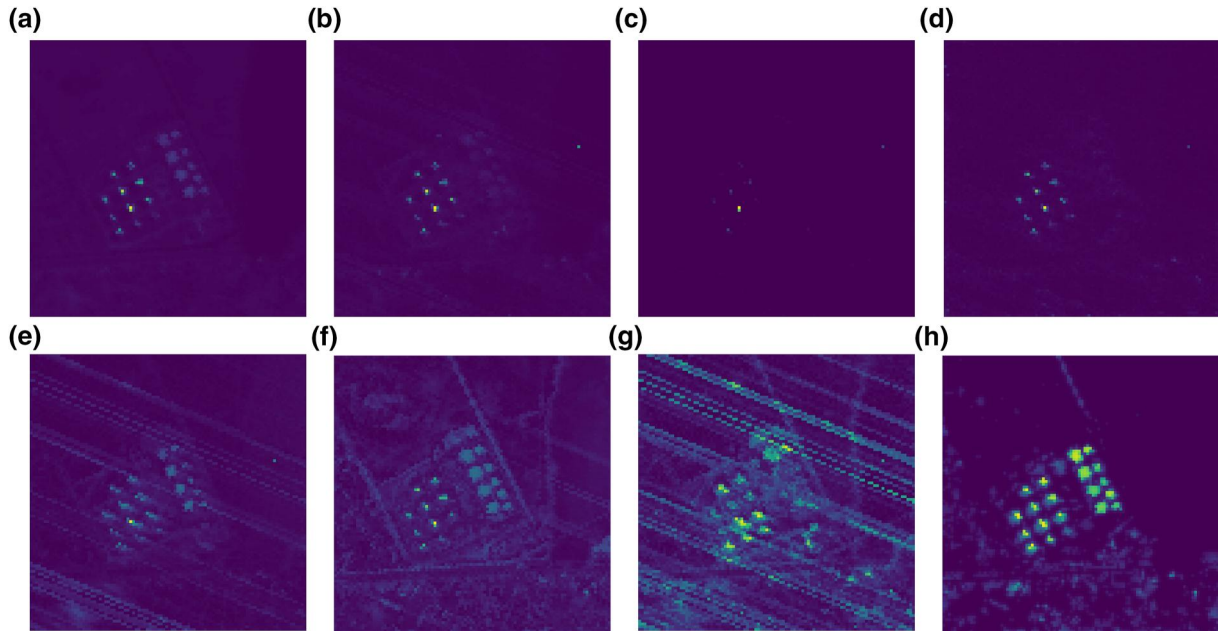
FIGURE 10 Detection maps on the Texas Coast data set. (a) memory-augmented autoencoder for hyperspectral anomaly detection (MAENet). (b) GRX. (c) local RX detector (LRX). (d) collaborative representation theory (CRD). (e) LRASR. (f) DAEAD. (g) KIFD. (h) AED

FIGURE 11 Detection maps on the Texas Coast data set. (a) memory-augmented autoencoder for hyperspectral anomaly detection (MAENet). (b) GRX. (c) local RX detector (LRX). (d) collaborative representation theory (CRD). (e) LRASR. (f) DAEAD. (g) KIFD. (h) AED
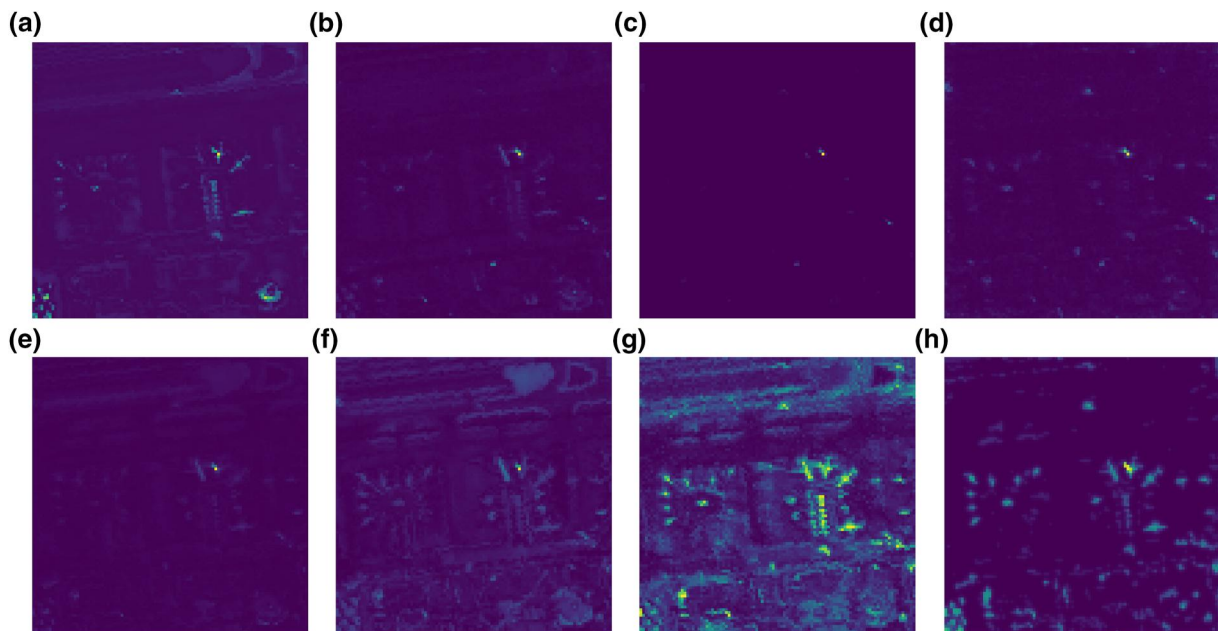
Overall, the ROC curves, AUC values and detection maps of the proposed method are better than those of other methods on the AVIRIS-II data set, which demonstrates the superiority of our MAENet.

(3) Detection Results on EI Segundo Data Set. The detection results of the EI Segundo data set are shown in Figure 9. The GRX, LRX, and CRD methods can detect a few anomalies, and the shapes of some targets are missing. Compared with GRX, the LRASR and DAEAD methods

can find out the locations of the anomalies and obtain better results, but they fail to suppress the background. The KIFD, AED and MAENet can detect almost all the anomalies, and the shapes of the targets are relatively clear. In particular, a few background samples are also detected as anomalies by KIFD and AED, but the MAENet can suppress the background well. It is noticeable that the intensity of anomalies of MAENet are weak. The main reason is that anomalies occur with a relatively high probability in this data set, and the memory items may
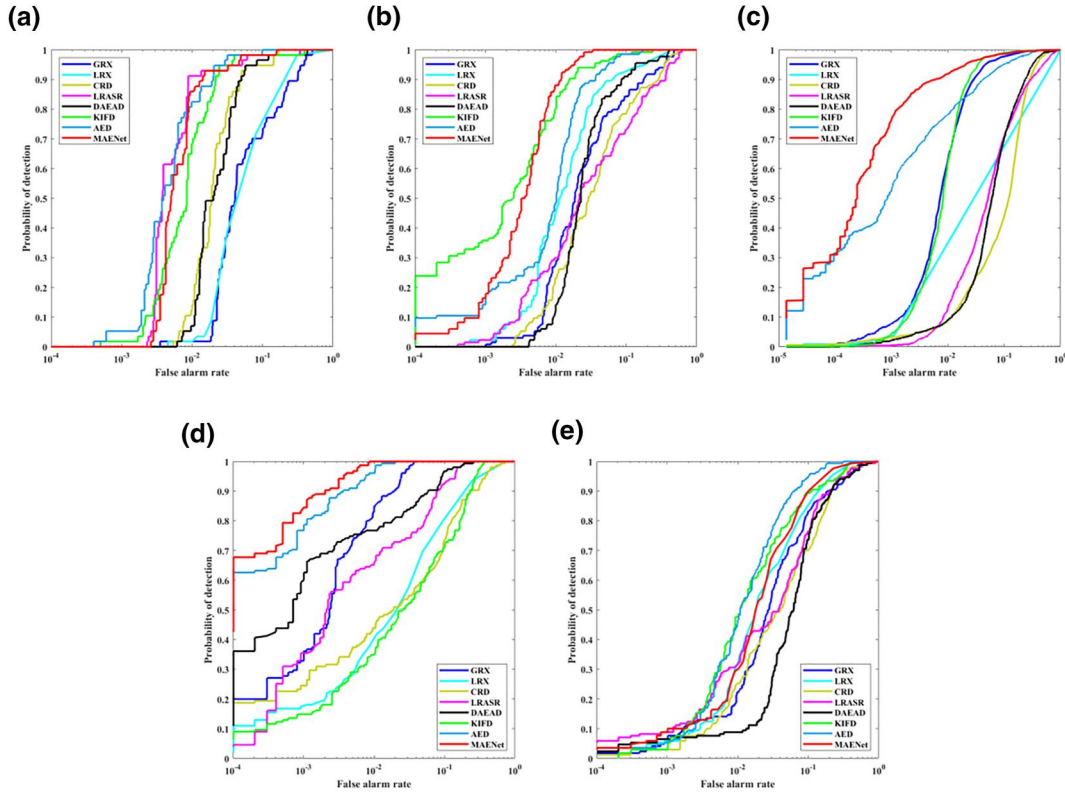
FIGURE 12 ROC curves of five data sets under different compared methods. (a) AVIRIS-I data set. (b) AVIRIS-II data set. (c) EI Segundo data set. (d) Texas Coast data set. (e) Los Angeles-3 set

TABLE 3 AUC values for eight detectors on five data sets

Methods	Data sets				
	AVIRIS-I	**AVIRIS-II**	**EI segundo**	**Texas coast**	**Los angeles**
GRX	0.9055	0.9403	0.9841	0.9946	0.9288
LRX	0.9391	0.9680	0.9369	0.9092	0.9506
CRD	0.9721	0.9236	0.8633	0.9181	0.9167
LRASR	0.9871	0.9097	0.8888	0.9753	0.9228
DAEAD	0.9671	0.9573	0.9019	0.9839	0.9039
KIFD	0.9834	0.9912	0.9864	0.9242	0.9562
AED	0.9919	0.9846	0.9823	0.9987	0.9756
MAENet	0.9894	0.9949	0.9943	0.9994	0.9590

record some abnormal characteristics. Figure 12c and the fourth column of Table 3 show the ROC curves and AUC values of all methods on the EI Segundo data set. It is easy to find that the ROC curve of MAENet is more outstanding than that of other methods. Meanwhile, it also obtains the highest AUC scores, 0.9943.

(4) *Detection Results on Texas Coast Data Set.* Figure 10 shows the detection results of the Texas Coast data set. The RX methods can almost detect all the anomalies, but the shapes of anomalies are blurred. The LRX and CRD method can suppress background well, but the detection rate is lower. The LRASR and KIFD methods suffer from the stripe noises, thus failing to detect anomalies. The

DAEAD, AED and MAENet can well detect all the anomalies, and the shapes of anomalies are relatively clear. Compared with the DAEAD method, MAENet can well suppress the background and is close to the GT. Moreover, Figure 12d and the fifth column of Table 3 show the ROC curves and AUC values of all methods on the Texas Coast data set, respectively. It further demonstrates the superiority of the MAENet.

(5) *Detection Results on Los Angeles-3 Data Set.* For the Los Angeles-3 data set, the anomalies are numerous aeroplanes, and the image scene is more complex than other data sets. The detection maps of eight detectors are shown in Figure 11, and Table 3 shows their AUC values. The

TABLE 4 Computing time (in seconds) of different methods

| Methods | Data sets | | | | |
	AVIRIS-I	AVIRIS-II	EI segundo	Texas coast	Los angeles
GRX	0.0874	0.0690	0.6262	0.1540	0.1001
LRX	90.7443	170.1347	1136.8556	60.4251	72.5761
CRD	61.8691	2047.9703	8176.0018	875.2952	6.6521
LRASR	17.6758	22.4709	159.1032	22.9348	22.9758
DAEAD	69.4188	69.8172	108.1950	75.4716	82.1239
KIFD	37.6012	35.8467	188.4894	42.5889	14.7329
AED	0.3807	0.4960	1.6539	0.4493	0.4414
MAENet	447.2579	458.7579	54.2990	31.3362	391.9876

AED obtains the highest AUC values, and our MAENet gets the second AUC scores. From those detection maps, we can see that the RX, LRX, and LRASR detectors mostly cannot detect anomalies, and they get poor AUC values. The ROC curve in Figure 12e further demonstrates the performance of each algorithm, and our method is second only to the AED.

The competing time of the eight detectors are listed in Table 4, and the RX and AED detectors are faster than other methods. The window-based methods require much more time, such as the CRD detector. The main drawback of the deep-learning method is their training time, so the DAEAD and MAENet are slower than the RX detector.

(6) *Robustness Study.* To further verify the robustness of the proposed MAENet, we add Gaussian noise with different signal-to noise ratios (SNRs) to the Texas Coast data set, and the results are shown in Figure 13. From Figure 13, we can see that MAENet and AED algorithms are more robust to noise and have good detection accuracy at a relatively low SNR. For other detectors, they are susceptible to noisy images, and the detection accuracy decreases rapidly at low SNRs. In addition, MAENet achieves the highest AUC values at almost all different SNRs, thus demonstrating the robustness of the proposed MAENet.

(7) *Differences from existing methods.* In this paper, a memory-augmented autoencoder is proposed for hyperspectral anomaly detection (MAENet). The aim of MAENet is to increase the reconstruction error of abnormal samples while ensuring that the background can be reconstructed well, so as to improve the accuracy of anomaly detection. There are many works that exploit AE architecture for hyperspectral anomaly detection, such as Refs. [13, 58]. In Ref. [13], the authors used the manifold learning skill to constrain the processing of an encoder, and the local features of HSI can be learnt by the encoder. Then, the reconstructed HSI is obtained by the decoder, and the local reconstruction errors together with global reconstruction errors are utilised for anomaly detection. Similar to this approach, Fan et al. proposed a graph AE
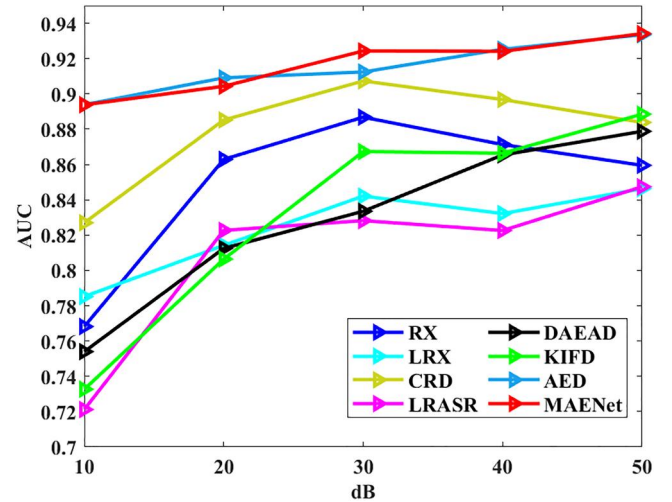

FIGURE 13 Robustness analysis using single Gaussian noise with the different signal-to noise ratios (SNRs) on the Texas Coast data set

for hyperspectral anomaly detection [58]. To maintain the geometric structure of the HSI, a graph constraint is added into the encoding space. Unlike those approaches, our MAENet reconstructs the encodings instead of constraining them. Afterwards, the aim of MAENet is to increase the reconstruction errors of abnormal samples, but not for learning the local features.

3.5 | Ablation study

In order to analyse the effect of loss function and memory module on the final detection result, an ablation study on the five data sets over the AUC scores is shown in Table 5. For simplicity, let L1 represent the original spectral reconstruction term in our loss function (i.e. $L1 = \|x_i - \widehat{x}_i\|_2^2$) and L2 represent the remaining part (i.e. $L2 = \|z_i - \widehat{z}_i\|_2^2$). There are three comparative experiments. In the first experiment, only the AE is used in the network architecture, where the reconstruction errors are applied for anomaly detection. In the

TABLE 5 The AUC scores of ablation study

Component	Data sets				
	AVIRIS-I	AVIRIS-II	EI segundo	Texas coast	Los angeles
AE	0.9838	0.9841	0.9679	0.9886	0.9386
MAE + L1	0.9885	0.9926	0.9915	0.9954	0.9501
MAE + L1+L2	0.9894	0.9949	0.9943	0.9994	0.9590

second experiment, the memory module is introduced into the AE architecture, and the AUC value of the EI Segundo data set is 0.9915, which can prove the superiority of the memory module. For the AVIRIS, Texas Coast and Los Angeles-3 data sets, the memory module can slightly improve the detection results. In the final experiment, the constraint between latent representation and the retrieved items is added into the loss function, then the performance is further improved. Overall, from those experiments, it can demonstrate the superiority of the loss function and memory module in the MAENet.

4 | CONCLUSION

In this paper, a memory AE network is introduced for hyperspectral anomaly detection (MAENet). Within MAENet, the background is reconstructed by an AE augmented with a memory module, and the anomalies are detected as the reconstruction errors. Different from previously mentioned AE-based methods, the encodings generated from the encoder are used as the query features to search for the most relevant items in the memory matrix by using an attention-based sparse addressing mechanism, and then the retrieved items are used for the decoder to reconstruct the original data set. Moreover, to guarantee the memory items can well represent the encodings, a self-perception loss is induced to highlight the reconstruction errors of anomalies while reconstructing the background samples well. Compared with other methods, the MAENet can obtain considerable results on five data sets. However, we also note that the proposed algorithm has limited detection accuracy for small and dense targets in the complex scenes, so how to improve the detection accuracy in the complex scenes is the main work in the future.

DATA AVAILABILITY STATEMENT
Data sharing is not applicable to this article as no new data were created or analysed in this study.

ORCID
Bangyong sun https://orcid.org/0000-0002-0265-1785

REFERENCES
1. Jiang, T., et al.: Discriminative reconstruction constrained generative adversarial network for hyperspectral anomaly detection. IEEE Trans. Geosci. Rem. Sens. 58(7), 4666–4679 (2020)
2. Zhang, B., et al.: Real-time target detection in hyperspectral images based on spatial-spectral information extraction. EURASIP Journal on Advances in Signal Processing, pp. 1–15 (2012)
3. Zheng, X., et al.: Unsupervised change detection by cross-resolution difference learning. IEEE Trans. Geosci. Rem. Sens. 60, 5606616 (2022). https://doi.org/10.1109/tgrs.2021.3079907
4. Guo, Q., et al.: Change detection for hyperspectral images via convolutional sparse analysis and temporal spectral unmixing. IEEE J. Sel. Top. Appl. Earth Obs. Rem. Sens. 14, 4417–4426 (2021). https://doi.org/10.1109/jstars.2021.3074538
5. Zheng, X., Yuan, Y., Lu, X.: A deep scene representation for aerial scene classification. IEEE Trans. Geosci. Rem. Sens. 57(7), 4799–4809 (2019)
6. Zhao, Z., et al.: Center attention network for hyperspectral image classification. IEEE J. Sel. Top. Appl. Earth Obs. Rem. Sens. 14, 3415–3425 (2021). https://doi.org/10.1109/jstars.2021.3065706
7. Hong, D., et al.: Graph convolutional networks for hyperspectral image classification. IEEE Trans. Geosci. Rem. Sens. 59(7), 5966–5978 (2020)
8. Wu, X., Hong, D., Chanussot, J.: Convolutional neural networks for multimodal remote sensing data classification. IEEE Trans. Geosci. Rem. Sens. 60, 5517010 (2022). https://doi.org/10.1109/tgrs.2021.3124913
9. Hong, D., et al.: Spectralformer: rethinking hyperspectral image classification with transformers. IEEE Trans. Geosci. Rem. Sens. 60, 5518615 (2022). https://doi.org/10.1109/tgrs.2021.3130716
10. Zheng, X., et al.: Rotation-invariant attention network for hyperspectral image classification. IEEE Trans. Image Proces Early Access, 1 (2022). https://doi.org/10.1109/TIP.2022.3177322
11. Shahid, K.T., Schizas, I.D.: Unsupervised hyperspectral unmixing via nonlinear autoencoders. IEEE Trans. Geosci. Rem. Sens. 60, 5506513 (2022). https://doi.org/10.1109/tgrs.2021.3077833
12. Li, F., et al.: Hyperspectral sparse unmixing with spectral-spatial low-rank constraint. IEEE J. Sel. Top. Appl. Earth Obs. Rem. Sens. 14, 6119–6130 (2021). https://doi.org/10.1109/jstars.2021.3086631
13. Lu, X., Zhang, W., Huang, J.: Exploiting embedding manifold of autoencoders for hyperspectral anomaly detection. IEEE Trans. Geosci. Rem. Sens. 58(3), 1527–1537 (2019)
14. Xie, W., et al.: Autoencoder and adversarial-learning based semi-supervised background estimation for hyperspectral anomaly detection. IEEE Trans. Geosci. Rem. Sens. 58(8), 5416–5427 (2020)
15. Zhang, L., Cheng, B.: A stacked autoencoders-based adaptive subspace model for hyperspectral anomaly detection. Infrared Phys. Technol. 96, 52–60 (2019). https://doi.org/10.1016/j.infrared.2018.11.015
16. Zhang, X., Wen, G., Dai, W.: A tensor decomposition-based anomaly detection algorithm for hyperspectral image. IEEE Trans. Geosci. Rem. Sens. 54(10), 5801–5820 (2016)
17. Wang, S., et al.: Auto-ad: autonomous hyperspectral anomaly detection network based on fully convolutional autoencoder. IEEE Trans. Geosci. Rem. Sens. 60, 5503314 (2022). https://doi.org/10.1109/tgrs.2021.3057721

18. Reed, I.S., Yu, X.: Adaptive multiple-band cfar detection of an optical pattern with unknown spectral distribution. IEEE Trans. Acoust. Speech Signal Process. 38(10), 1760–1770 (1990)

19. Matteoli, S., et al.: A locally adaptive background density estimator: an evolution for rx-based anomaly detectors. Geosci. Rem. Sens. Lett. IEEE. 11(1), 323–327 (2013)

20. Kwon, H., Nasrabadi, N.M.: Kernel rx-algorithm: a nonlinear anomaly detector for hyperspectral imagery. IEEE Trans. Geosci. Rem. Sens. 43(2), 388–397 (2005)

21. Guo, Q., et al.: Weighted-rxd and linear filter-based rxd: improving background statistics estimation for anomaly detection in hyperspectral imagery. IEEE J. Sel. Top. Appl. Earth Obs. Rem. Sens. 7(6), 2351–2366 (2014)

22. Li, Z., Zhang, Y.: A new hyperspectral anomaly detection method based on higher order statistics and adaptive cosine estimator. Geosci. Rem. Sens. Lett. IEEE. 17(4), 661–665 (2019)

23. Hidalgo, J.A.P., et al.: Efficient nonlinear rx anomaly detectors. Geosci. Rem. Sens. Lett. IEEE. 18(2), 231–235 (2021)

24. Zhang, W., Lu, X., Li, X.: Similarity constrained convex nonnegative matrix factorization for hyperspectral anomaly detection. IEEE Trans. Geosci. Rem. Sens. 57(7), 4810–4822 (2019)

25. Li, J., et al.: Hyperspectral anomaly detection by the use of background joint sparse representation. IEEE J. Sel. Top. Appl. Earth Obs. Rem. Sens. 8(6), 2523–2533 (2015)

26. Li, W., Du, Q.: Collaborative representation for hyperspectral anomaly detection. IEEE Trans. Geosci. Rem. Sens. 53(3), 1463–1474 (2014)

27. Ma, N., Peng, Y., Wang, S.: A fast recursive collaboration representation anomaly detector for hyperspectral image. Geosci. Rem. Sens. Lett. IEEE. 16(4), 588–592 (2018)

28. Zhao, C., et al.: Spectral-spatial anomaly detection via collaborative representation constraint stacked autoencoders for hyperspectral images. Geosci. Rem. Sens. Lett. IEEE. 19, 5503105 (2022). https://doi.org/10.1109/lgrs.2021.3050308

29. Cheng, T., Wang, B.: Total variation and sparsity regularized decomposition model with union dictionary for hyperspectral anomaly detection. IEEE Trans. Geosci. Rem. Sens. 59(2), 1472–1486 (2021)

30. Zhang, Y., et al.: A low-rank and sparse matrix decomposition-based mahalanobis distance method for hyperspectral anomaly detection. IEEE Trans. Geosci. Rem. Sens. 54(3), 1376–1389 (2015)

31. Xu, Y., et al.: Anomaly detection in hyperspectral images based on low-rank and sparse representation. IEEE Trans. Geosci. Rem. Sens. 54(4), 1990–2000 (2015)

32. Qu, Y., et al.: Hyperspectral anomaly detection through spectral unmixing and dictionary-based low-rank decomposition. IEEE Trans. Geosci. Rem. Sens. 56(8), 4391–4405 (2018)

33. Zhang, X., et al.: Spectral-difference low-rank representation learning for hyperspectral anomaly detection. IEEE Trans. Geosci. Rem. Sens. 59(12), 10364–10377 (2021)

34. Feng, S., et al.: A hyperspectral anomaly detection method based on low-rank and sparse decomposition with density peak guided collaborative representation. IEEE Trans. Geosci. Rem. Sens. 60, 5501513 (2022). https://doi.org/10.1109/tgrs.2021.3054736

35. Fu, X., et al.: Hyperspectral anomaly detection via deep plug-and-play denoising cnn regularization. IEEE Trans. Geosci. Rem. Sens. 59(11), 9553–9568 (2021)

36. Zheng, X., et al.: Mutual attention inception network for remote sensing visual question answering. IEEE Trans. Geosci. Rem. Sens. 60, 5606514 (2022). https://doi.org/10.1109/tgrs.2021.3079918

37. Zheng, X., et al.: Generalized scene classification from small-scale datasets with multitask learning. IEEE Trans. Geosci. Rem. Sens. 60, 5609311 (2022). https://doi.org/10.1109/tgrs.2021.3116147

38. Yuan, Y., Xiong, Z., Wang, Q.: Vssa-net: vertical spatial sequence attention network for traffic sign detection. IEEE Trans. Image Process. 28(7), 3423–3434 (2019)

39. Wang, Q., Li, Q., Li, X.: A fast neighborhood grouping method for hyperspectral band selection. IEEE Trans. Geosci. Rem. Sens. 59(6), 5028–5039 (2021)

40. Wang, Q., et al.: Getnet: a general end-to-end 2-d cnn framework for hyperspectral image change detection. IEEE Trans. Geosci. Rem. Sens. 57(1), 3–13 (2019)

41. Xie, W., et al.: Unsupervised spectral mapping and feature selection for hyperspectral anomaly detection. Neural Network. 132, 144–154 (2020). https://doi.org/10.1016/j.neunet.2020.08.010

42. Ma, N., et al.: An unsupervised deep hyperspectral anomaly detector. Sensors. 18(3), 693 (2018). https://doi.org/10.3390/s18030693

43. Zhao, C., Li, X., Zhu, H.: Hyperspectral anomaly detection based on stacked denoising autoencoders. J. Appl. Remote Sens. 11(4), 042605 (2017). https://doi.org/10.1117/1.jrs.11.042605

44. Zhao, C., Zhang, L.: Spectral-spatial stacked autoencoders based on low-rank and sparse matrix decomposition for hyperspectral anomaly detection. Infrared Phys. Technol. 92, 166–176 (2018). https://doi.org/10.1016/j.infrared.2018.06.001

45. Chang, S., Du, B., Zhang, L.: A sparse autoencoder based hyperspectral anomaly detection algorithm using residual of reconstruction error. In: IGARSS 2019-2019 IEEE International Geoscience and Remote Sensing Symposium, pp. 5488–5491. IEEE (2019)

46. Lei, J., et al.: Spectral–spatial feature extraction for hyperspectral anomaly detection. IEEE Trans. Geosci. Rem. Sens. 57(10), 8131–8143 (2019)

47. Bangyong, S., et al.: Hyperspectral anomaly detection based on 3d convolutional autoencoder and low rank representation. Acta Photonica Sin. 50(4), 0410003 (2021)

48. Zhang, J., et al.: Anomaly detection in hyperspectral image using 3d-convolutional variational autoencoder. In: 2021 IEEE International Geoscience and Remote Sensing Symposium IGARSS, pp. 2512–2515. IEEE (2021)

49. Jiang, K., et al.: Semisupervised spectral learning with generative adversarial network for hyperspectral anomaly detection. IEEE Trans. Geosci. Rem. Sens. 58(7), 5224–5236 (2020)

50. Xie, W., et al.: Spectral adversarial feature learning for anomaly detection in hyperspectral imagery. IEEE Trans. Geosci. Rem. Sens. 58(4), 2352–2365 (2019)

51. Gong, D., et al.: Memorizing normality to detect anomaly: memory-augmented deep autoencoder for unsupervised anomaly detection. In: Proceedings of the IEEE/CVF International Conference on Computer Vision, pp. 1705–1714. IEEE (2019)

52. Huber-Lerner, M., et al.: Hyperspectral band selection for anomaly detection: the role of data gaussianity. IEEE J. Sel. Top. Appl. Earth Obs. Rem. Sens. 9(2), 732–743 (2015)

53. Kang, X., et al.: Hyperspectral anomaly detection with attribute and edge-preserving filters. IEEE Trans. Geosci. Rem. Sens. 55(10), 5600–5611 (2017)

54. Manolakis, D., et al.: Detection algorithms in hyperspectral imaging systems: an overview of practical algorithms. IEEE Signal Process. Mag. 31(1), 24–33 (2013)

55. Kingma, D.P., Ba, J.: Adam: A Method for Stochastic Optimization (2014). arXiv preprint arXiv:14126980

56. Taghipour, A., Ghassemian, H.: Unsupervised hyperspectral target detection using spectral residual of deep autoencoder networks. In: 2019 4th International Conference on Pattern Recognition and Image Analysis (IPRIA), pp. 52–57. IEEE (2019)

57. Li, S., et al.: Hyperspectral anomaly detection with kernel isolation forest. IEEE Trans. Geosci. Rem. Sens. 58(1), 319–329 (2019)

58. Fan, G., et al.: Hyperspectral anomaly detection with robust graph autoencoders. IEEE Trans. Geosci. Rem. Sens. 60, 5511314 (2022). https://doi.org/10.1109/tgrs.2021.3097097